Pressure-induced electride phase formation in calcium: A key to its strange high-pressure behavior

P. Modak* and Ashok K. Verma
High Pressure & Synchrotron Radiation Physics Division, Bhabha Atomic Research Centre, Mumbai-400085, India
Homi Bhabha National Institute, Anushaktinagar, Mumbai-400 094, India

Peter M. Oppeneer
Department of Physics and Astronomy, Uppsala University, P.O. Box 516, SE-75120 Uppsala, Sweden

(Received 16 September 2022; accepted 13 March 2023; published 28 March 2023)

Elemental calcium (Ca), a simple metal at ambient conditions, has attracted huge interest because of its unusual high-pressure behavior in structural, electrical, and melting properties whose origins remain unsolved. Here, using a theoretical framework appropriate for describing electride phase formation, i.e., the presence of anionic electrons, we establish electride formation in Ca at a pressure as low as 8 GPa. Our analysis shows that under pressure the valence electrons of Ca localize at octahedral holes and exhibit anionic character which is responsible for its strange pressure behavior. Our calculated enthalpy and electrical resistance indicate that Ca will directly transform from an fcc-electride phase to a simple cubic sc-electride phase near 30 GPa, thereby avoiding the intermediate bcc phase. These findings are not limited to Ca but might hold a key to the understanding of host-guest type structures which occur in other elemental solids, though at much higher pressures.

DOI: 10.1103/PhysRevB.107.125152

I. INTRODUCTION

Calcium exhibits strange high-pressure behavior in the 8–50 GPa pressure region [1–12]. The room-temperature electrical resistance of Ca shows a continuous increase from 8 to 18 GPa; then it gradually decreases, attaining a lowest value near 25 GPa and afterwards it again starts increasing, attaining the highest value near 42 GPa which is highly unusual for a good metal like Ca [2]. Subsequent x-ray diffraction (XRD) measurements advocated a face-centered cubic (fcc) to body-centered cubic (bcc) structural transition near 19.2 GPa, and then a bcc to simple cubic (sc) transition near 33 GPa which is, however, contrary to the widely accepted high-pressure structural behavior of most materials that are expected to adopt progressively more and more close-packed structures under compression [3]. The occurrence of bcc structure near 19.2 GPa is also abnormal as bcc is a high-temperature ambient-pressure phase which has a good metallic nature at all pressures and hence this phase cannot explain the observed resistance behavior [2]. The experimental assignment of the bcc phase, near 19.2 GPa, is based on the fact that a single equation of state could be adopted for both an unknown phase and ambient-pressure high-temperature bcc phase [3]. A recently claimed bcc observation was also not totally convincing [6] since the most prominent peak, indexed as (111), for bcc Ca in the XRD pattern will have zero value for the structure factor. Further, all high-pressure experiments were carried out under nonhydrostatic conditions which may strongly influence the phase-transition kinetics. A large transition pressure mismatch between the experimental and theoretical results was furthermore reported for the fcc to bcc transition [3–7,10–12]. Moreover, the experimental observation of sc Ca is controversial as quasiharmonic phonon calculations using semilocal functionals gave imaginary phonon frequencies for sc Ca at 0 K [8,9,12]. Subsequent crystal structure searches found a tetragonal $I4_1/amd$ [body-centered tetragonal (bct)] structure which becomes energetically favorable over sc near 34 GPa [10]. Although several theoretical approaches have been applied to resolve the structural inconsistency between theory and experiments, a consistent phase diagram of Ca is still missing in the 0–50 GPa region [11–15].

Further, Ca was proposed to adopt a host-guest type structure above 134 GPa [16]. It is worth mentioning that startling complexities were observed in simple elemental solids under high pressure. Some elements adopt a nonperiodic incommensurate/host-guest structure; in some cases, the elements show spectacular changes in physical properties at high pressures. Barium metal, for example, adopts a highly complex host-guest structure near 12 GPa and metals such as Li, Na, K, Mg, and Cs turn into a semimetal or insulator when subjected to extreme high pressures [17–22]. It is widely believed that under extreme pressures these form electrides, an unusual class of materials containing localized electrons at the non-nuclear sites, i.e., at interstitial sites which act like an anion [17–21,23,24]. There are several alkali and alkali-earth metals containing compounds which host electride phases at ambient conditions [25–29] but an elemental electride is unknown. Identification of an electride in Ca may allow experiments to explore the role of anionic electrons for complex phase formation in an elemental solid at low pressures.

In this work, using a hybrid exchange-correlation functional known to give correct descriptions for localized

*Corresponding author: paritoshmodak295@gmail.com

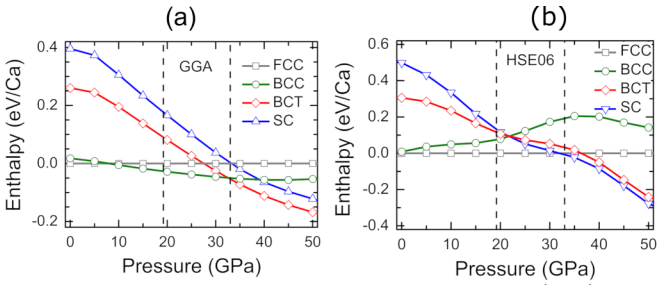

FIG. 1. Calculated high-pressure solid-solid structural phase transitions in Ca. (a), (b) Pressure variation of enthalpy for bcc, bct, and sc phases relative to the ambient fcc phase. Vertical dashed line represents experimental phase boundaries (fcc to bcc at 19.2 GPa and bcc to sc at 33 GPa) at room temperature.

electrons, we explore the possibility of electride formation in Ca and establish the formation of such phase at 8 GPa. Since experimental detection of the interstitial anionic electrons is not straightforward under high pressures, electron density based descriptors such as Bader analysis [30], electron-localization function (ELF) [31], and the presence of non-nuclear maxima and their charge content are usually used to detect the electride phase in solids. We adopt this methodology and obtain clear indicators of a Ca electride phase at 8 GPa. Our results demonstrate that a bcc phase would not exist in Ca at high pressures at 0 K when we correctly treat its localized anionic electrons. Also, the calculated resistance for electride fcc Ca reproduces the measured high-pressure electrical resistance data satisfactorily, explaining Ca's strange resistivity behavior.

II. METHODOLOGY

To establish pressure-induced electride formation, we calculated total energy, ELFs, Bader charges, and band-decomposed charge density using the Vienna *Ab Initio* Simulation Package (VASP) for different phases at different pressures [32–34]. The projector augmented wave potential with configuration $3s^2 3p^6 4s^2$ is used in conjunction with 346.6 eV effective cutoff for a plane wave basis set [35]. For exchange correlation, the generalized gradient approximation (PBE-GGA) and Heyd-Scuseria-Ernzerhof (HSE06) hybrid functional are used [36,37]. It is worth mentioning, in connection to the localization of valence electrons, that large overdelocalization errors are expected for semilocal density functionals such as GGA, whereas hybrid functionals are expected to give a proper description of such systems. A $36\times36\times36$ k-point grid is used for Brillouin zone sampling for the cubic structures and equivalent Δk (~ 0.03 Å^{-1}) is used for noncubic structure. Electronic charge density critical points are calculated using the CRITIC2 program [38]. A $4\times4\times4$ supercell is used for phonon calculations [39].

III. RESULTS AND DISCUSSIONS

In Fig. 1, we present our pressure-enthalpy data of the fcc, bcc, sc, and bct phases of Ca. The obtained zero-pressure properties with both types of functionals compare fairly well with previous theoretical and experimental results as shown in Table I. However, it is worth mentioning that the HSE06 gives a much better estimation of these quantities. Analogous to earlier studies, the GGA functional gives an fcc to bcc transition near 8.2 GPa and bcc to bct transition near 27.6 GPa and there is no sign of a stable sc phase up to 50 GPa [10,11,16], contrary to what has been observed in the experiments [3–6]. This excellent matching with earlier theoretical works [10,14,16] establishes the reliability of our calculations and chosen parameters such as energy cutoff, k-point grid, etc. Remarkably, HSE06 predicts an fcc to sc transition near 30 GPa whereas bcc and bct structures remain unfavorable up to 50 GPa [see Fig. 1(b)]. This contrasting phase stability behavior compared to GGA may result from the inability of the GGA functional to treat localized charge density which was predicted to exist in Ca but at high pressure [16]. It is important to note that an earlier study with a hybrid functional has not shown the fcc stability region but gave a stable bcc phase in the 20–28 GPa pressure region, a bct phase in the 28–33 GPa pressure region, and an sc phase above 33 GPa [15]. In reality the actual phase transition not only depends on the energetics but also on the phase-transition kinetics which is absent in our calculations at 0 K. It is to be noted that in high-pressure experiments with diamond anvil cell (DAC), the phase-transition kinetics strongly depends on the temperature, presence of impurity, and compression such as hydrostatic or nonhydrostatic. In many systems, it was observed that phase-transition pressure and phase sequence are strongly influenced by the presence of nonhydrostatic stresses [42–44]. The experimental observation of the bcc phase near 20 GPa in Ca might have occurred due to the presence of strong nonhydrostatic stresses as all experiments were carried out either with dried KCl disks as pressure transmitting medium or without any pressure transmitting medium [3,4,6]. Furthermore, our computed enthalpy curves reveal that the bcc phase might stabilize in the negative-pressure region, consistent with the fact that bcc has been observed at ambient-pressure, high-temperature conditions [45].

TABLE I. Comparison of calculated equilibrium volume and bulk modulus of Ca with those of experiments [40,41].

	Equilibrium volume (Å^3)	Bulk modulus (GPa)
GGA	41.68	21.40
HSE06	42.99	18.70
Experiment [40,41]	43.53	15.2

To examine electride phase formation in Ca we analyzed ELF, a strong indicator for an electride phase. It takes values between 0 and 1.0 where the value 1.0 corresponds to the perfect localization limit and the value 0.5 represents the homogeneous electron gas limit which is best described by semilocal functionals such as local density approximation (LDA) and GGA [46,36]. Thus, systems containing high ELF values are prone to an overdelocalization error when treated by semilocal functionals.

Figures 2(a) and 2(b) present ELF data for fcc and sc structures. It is evident that for these structures the highest ELF occurs at non-nuclear interstitial sites (octahedral holes). For the GGA functional, we find that the ELF value increases from

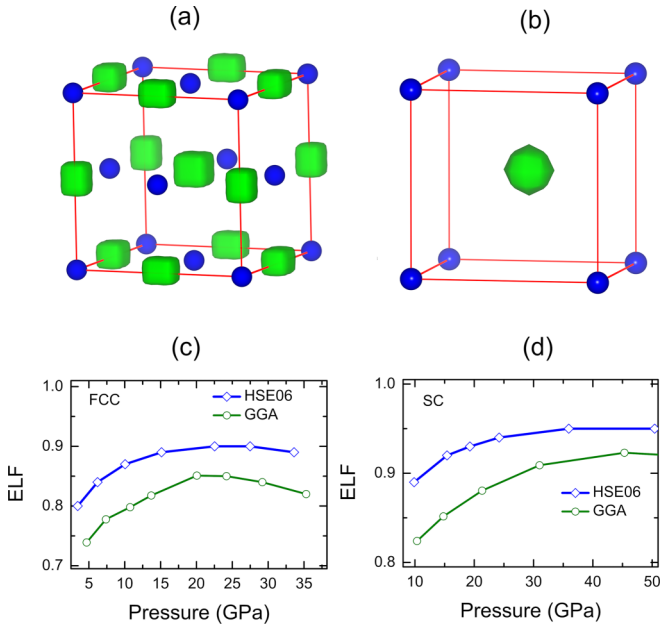

FIG. 2. Computed ELFs of fcc and sc Ca for HSE06 functional. (a) fcc Ca ELF surface for an isovalue = 0.80, near 10 GPa; (b) sc Ca ELF surface for an isovalue = 0.88, near 32 GPa. Here, small blue balls represent Ca atoms and ELF surfaces are shown in green. (c), (d) Pressure dependence of the highest ELF values of fcc and sc Ca, respectively.

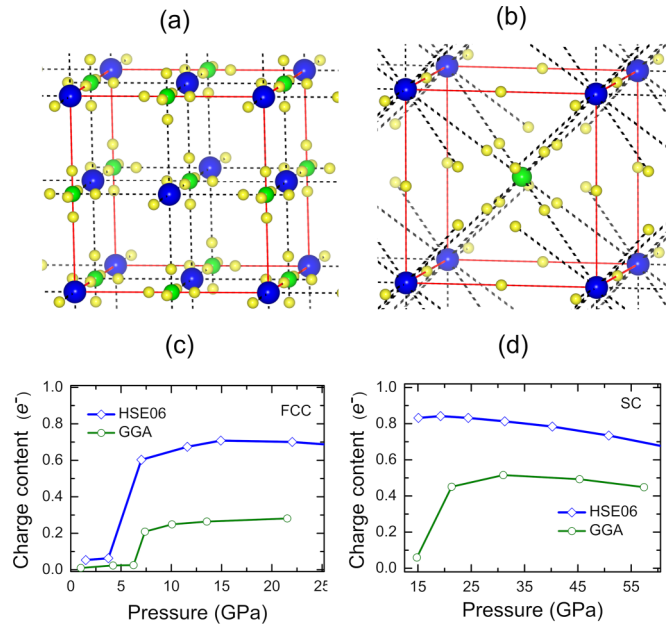

FIG. 3. NNM and bcp of Ca under pressure calculated using the HSE06 functional. (a) NNM at octahedral holes (green balls), and bcp (yellow balls) in fcc Ca near 15 GPa. (b) NNM (green balls) and bcp (yellow balls) in sc Ca near 34 GPa. Here, blue balls represent Ca atoms. (c), (d) Pressure dependence of NNM charge content at octahedral holes in fcc and sc phases.

0.70 to 0.85 for fcc structure in the 0–21 GPa pressure interval, and on further compression the ELF value gradually decreases [Fig. 2(c)]. With the HSE06 functional, the highest ELF value varies from 0.85 to 0.90 in the 8–22 GPa pressure region. For the sc phase, the highest ELF value varies from 0.85 to 0.92 in the case of GGA and from 0.93 to 0.95 in the case of HSE06 over the 20–45 GPa pressure interval [Fig. 2(d)]. For the bcc structure, the ELF has comparatively lower values and, importantly, the highest value, 0.70, occurs in the vicinity of atomic sites and remains practically independent of the pressure for both functionals (shown in Fig. S1(a) in the Supplemental Material [47]). Notably, the bcc structure exhibits no interstitial charge localization at any pressure. The bct structure also exhibits interstitial electron localization (shown in Fig. S1(b) [47]) and the highest ELF value varying from 0.80 to 0.82 for HSE06 in the pressure region of 20–35 GPa. The occurrence of interstitial charge localization in fcc, sc, and bct structures indicates the likelihood of electride formation under favorable conditions. The ELF analysis explicitly establishes further that a large electron overdelocalization error is unavoidable for fcc and sc structures when using semilocal functionals since these structures possess a very high value of ELF in their octahedral holes. Thus, semilocal functionals used in earlier studies have underestimated the fcc stability region. It is also highly possible that the overdelocalization error of semilocal functionals has contributed to the predicted dynamical instability of the sc structure whose existence was, however, convincingly shown by several experiments [3–6].

Next, we analyze the critical points (CPs) of the crystal electron charge density characterized by zero gradient of the electron density [48]. There are four types of CPs, namely, local minimum or cage CP (ccp), local maximum or nuclear CP (ncp), and two kinds of saddle points, bond CP (bcp) and ring CP (rcp). A charge density minimum (maximum) is associated with positive (negative) curvatures of the field lines in all three directions; bcp has two negative curvatures and rcp has one negative curvature out of three. The occurrence of a charge density local maximum in the interstitial region, i.e., a non-nuclear maximum (NNM), is another strong indicator of an electride phase formation provided it has significant charge content (>10% of the valence charge) [49]. We estimated the NNM charge content using the Yu-Trinkle algorithm, as implemented in the CRITIC2 program [50,38]. We found that the fcc phase has NNMs at both tetrahedral holes and the region surrounding octahedral holes below 8 GPa (shown in Fig. S2 [47]). However, these NNMs have relatively small charge content, $0.004e^-$ at tetrahedral holes and $0.02e^-$ around octahedral holes. We observed that close to 8 GPa the NNMs at tetrahedral holes vanish and NNMs around the octahedral hole merge and move right at the octahedral position [shown in Fig. 3(a)], which was also reported in an earlier study [51]. Charge content of this NNM is $0.25e^-$ for GGA and $0.60e^-$ for HSE06. This confirms the interstitial anion formation which is also known as an interstitial quasiatom (ISQ). Thus, our analysis establishes electride phase formation in the fcc structure. Furthermore, it is evident from Fig. 3(a) that the bond CPs are located between Ca and the ISQ sites indicating dominant interactions between Ca and ISQ. It is pertinent to mention that an earlier study named this transition an isostructural transition [51]. However, it is apparent from our analysis that the electride phase formation represents a phase transition from fcc to a NaCl (B1) type pseudobinary

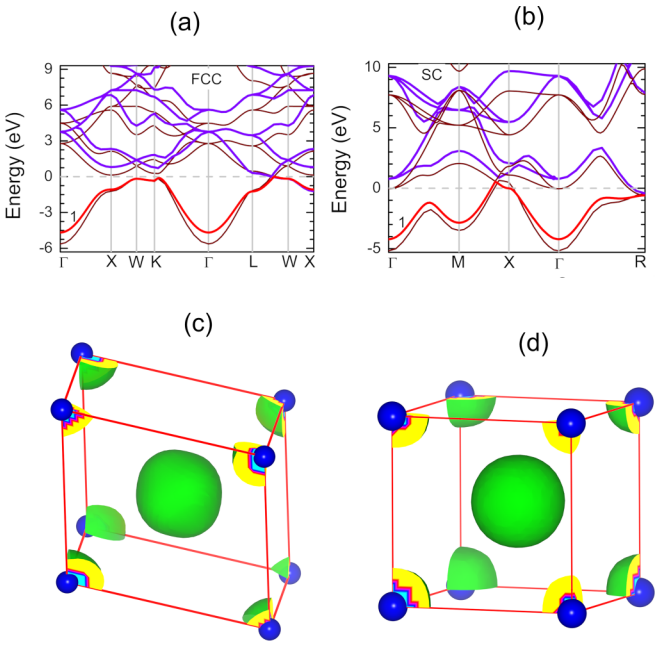

FIG. 4. Electronic band structure and electride charge density surfaces. (a) fcc Ca band structure near 14 GPa; (b) sc Ca band structure near 40 GPa. Here, thin brown curves represent GGA bands, whereas thick violet and red curves represent HSE06 bands. (c) fcc Ca HSE06 band-decomposed charge density surface for an isovalue = $0.07e^-$. (d) As in (c), but for sc Ca for an isovalue = $0.15e^-$.

phase, i.e., an ionic solidlike behavior above 8 GPa. On further compression, the charge content of this ISQ increases, reaching a value of $0.46e^-$ for GGA and $0.71e^-$ for HSE06 near 20 GPa; afterward its charge content starts decreasing [shown in Fig. 3(c)]. This is consistent with the observed electrical resistance behavior [2].

From a similar analysis, we find that the sc structure also has NNM at octahedral holes and their charge content near 30 GPa is $0.52e^-$ for GGA and $0.81e^-$ for HSE06 [shown in Fig. 3(b)]. The NNM charge content gradually decreases with pressure [shown in Fig. 3(d)]. This establishes that the sc phase also forms an electride phase, analog to a pseudobinary CsCl (B2) type solid. Remarkably, the bcc structure does not have NNMs whereas the bct structure has NNMs but their charge content is exceptionally small. Thus, we anticipate that Ca in bcc and bct structures will exhibit good metal behavior. It is further worthwhile to mention the striking resemblance of the high-pressure melting behavior of Ca and NaCl solid [52,53] where both materials show a nearly flat melting curve in the 10–30 GPa pressure interval and then exhibit a sudden rise in melting temperature near 30 GPa, a pressure value which is close to the B1-B2 transition of the NaCl solid.

The existence of anionic electrons in a solid usually results in a high-lying partially occupied state in its electronic band structure. For fcc and sc phases, this state hybridizes with the atomic s state and lies close to the Fermi level (E_F). Moreover, this state pushes up the $3d$ states, away from the Fermi level as evident from the electronic band structure with HSE06, shown in Figs. 4(a) and 4(b) and thus reducing the possibility of $3d$ occupancy. Therefore, our findings strongly indicate that the long-held pressure-induced s to d electron transfer in Ca is not correct. Additionally, to support the presence of the electride state we have calculated band-decomposed charge density which evidently shows that the partially occupied band, as indicated by red in Figs. 4(a) and 4(b), is associated with the anionic electrons that are shown in Figs. 4(c) and 4(d). To show the electride state in a further way we have calculated band structure using tight-binding linear muffin-tin orbital (TB-LMTO) method [54] by putting an empty sphere (E) which acts as a replica of ISQ, at the octahedral hole of both phases. The fat band plots, shown in Fig. S3 in the Supplemental Material [47], are associated with the empty sphere which, too, proves the presence of an electride state.

To gain insight in chemical bonding in the electride phases of Ca, we have computed the crystal orbital Hamiltonian population (COHP) [55] and its integrated value (ICOHP) under pressure for fcc and sc phases using the TB-LMTO code [54]. Negative COHP values indicate a bonding interaction, whereas positive values indicate an antibonding interaction and the ICOHP up to the Fermi energy gives an estimate of the bond strength [55].

For both phases, we find that the Ca-Ca pair has much smaller COHP and ICOHP values in comparison to that of Ca-E pair, indicating an effective chemical bonding between Ca and ISQ (shown in Figs. S4(a) and S4(b) [47]). This agrees with our charge density critical point analysis where we found bond paths between Ca and ISQ sites. This analysis further supports that the chemical bonding in Ca metals above 8 GPa is through interactions between Ca^+ at atomic sites and anionic electrons located at octahedral holes, i.e., effectively an ionic interaction analogous to Na^+-Cl^- in the fcc and Cs^+-Cl^- in the sc structure. For both phases the chemical bond strength shows an increasing trend with increase of pressure (see Figs. S4(c) and S4(d) [47]).

To examine the dynamical stability of the electride sc Ca structure we carried out phonon calculations with HSE06. We found dynamically stable sc Ca at 0 K above 30 GPa (shown in Fig. S5 [47]) contrary to earlier calculations with a semilocal functional which reported imaginary phonon frequencies for sc Ca at high-pressure conditions at 0 K, thereby questioning previously the existence of sc Ca [8,9,12].

Next, to understand the observed electrical resistance behavior, we used the Bloch resistivity formula, considering electrons have parabolic dispersions and are scattered by Debye phonons [56]. Although the Bloch resistivity formula was devised for free electron metals, it has been observed that the theory is amazingly powerful and surprisingly accurate for a wide class of materials [57]. For many metals the Bloch resistivity formula is used to extract electron-phonon coupling constants (λ) from measured resistivity data and calculated squared Drude plasma frequencies (ω_p^2). For metals such as In, Sn, Nb, V, Pb, etc., the extracted electron-phonon coupling constant matches exceptionally well with those of tunneling measurements. An interesting aspect is that the electron-phonon coupling constant for Pb is as high as 1.5 [58] which is also well reproduced by the Bloch resistivity formula [59]. For anisotropic or non-Debye cases, it is necessary to include general phonon dispersions which can be done by using the Eliashberg function $\alpha^2F(\omega)$. However, it was observed that except at low temperatures, the Bloch resistivity is not

particularly sensitive to the form of $\alpha^2F(\omega)$ [57]. Hence, this justifies the use of the Bloch resistivity formula in our case, too. It is to be noted that the Bloch formula accounts only for normal processes of electron-phonon scattering. Except at very low temperatures an umklapp process may become important. The probability of an umklapp process depends both on the size of the Fermi sheets and the distance between two sheets in neighboring zones. From our calculated band structure of fcc Ca near 14 GPa [Fig. 4(a)] it is evident that partially occupied bands cross the Fermi level along the L-W direction of the Brillouin zone (BZ) where the L point is the center and the W point is the corners of the hexagonal face of this zone. Thus, a ringlike narrow Fermi sheet around the L point on this hexagonal face is expected for fcc Ca as obtained in earlier calculations with the GGA functional [60]. Also, Fermi sheets at two neighboring zones will be far apart as they occur at the zone boundary. Therefore the probability of umklapp scattering is expected to be small because a phonon of higher energy is needed to drive the electron over a longer distance to land on another Fermi surface in a neighboring BZ.

Assuming isotropic compression one can convert the resistivity into resistance and then the normalized resistance can be written as

$$\frac{R_P}{R_0} = \left(\frac{V_P}{V_0}\right)^{3/2} \left(\frac{\theta_D^0}{\theta_D^P}\right)^6 \frac{I_5(x_P)}{I_5(x_0)} \frac{N_0(E_F)}{N_P(E_F)}, \tag{1}$$

where $x = \theta_D/T$ and $I_5(x) = \int_0^x \frac{z^5 e^z}{(e^z-1)^2} dz$. Here "0" refers to quantities at zero pressure and "P" refers to the corresponding quantity at pressure P GPa. $N(E_F)$ is the DOS at E_F per unit cell having volume V. Since Ca bands close to E_F have considerable dispersions, we can safely use this formula. We calculated the Debye temperature θ_D at different pressures and temperatures by computing the phonon DOS and then taking the second-order moment of the phonon frequencies; they are presented in Table S1 in the Supplemental Material [47]. Figure 5 shows the pressure variation of normalized resistance for GGA and HSE06 functionals along with the experimental data. To check the effect of electronic temperature on resistance we calculated the electronic DOS using Fermi-Dirac smearing with widths of 100 and 300 K and also Methfessel-Paxton smearing with width 0.1 eV for GGA (shown in Fig. S6(a) [47]). It is evident that GGA can explain the first peak in the observed pressure variation of resistance but fails above 20 GPa. The right shift of the first peak with temperature is also reproduced by GGA. As the pressure variation of resistance is nearly identical for Fermi-Dirac smearing corresponding to 300 K and Methfessel-Paxton smearing with width 0.1 eV, we used the latter one for computing electronic DOS with the HSE06 (see Fig. S6(b) [47]). The computed pressure variation of resistance for HSE06 agrees well with that of the observed behavior at 300 K. It is evident from Fig. 5 that the normalized resistance of bcc Ca does not follow the observed behavior indicating an improper assignment of this structure in the pressure range of 0–50 GPa.

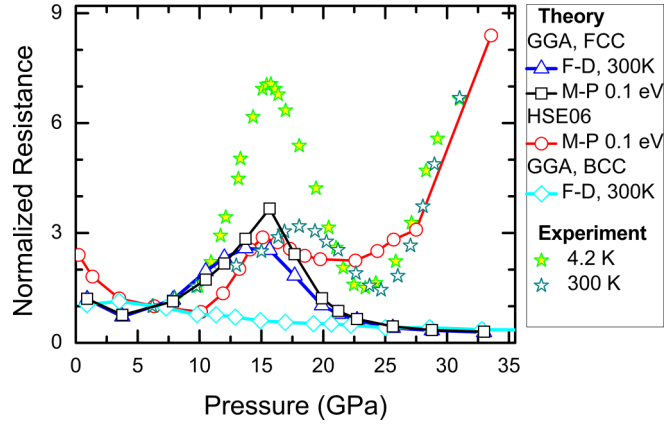

FIG. 5. Pressure variation of electrical resistance of Ca up to 35 GPa. Experimental data are from Ref. [2]. Here, F-D stands for Fermi-Dirac smearing and M-P stands for Methfessel-Paxton smearing methods.

IV. CONCLUSIONS

In summary, we have shown that electride phase formation is responsible for the strange high-pressure behavior of Ca. Under compression Ca forms an fcc NaCl-type electride near 8 GPa, which transforms to another sc CsCl-type electride phase near 30 GPa, thereby completely skipping a bcc phase. Our analysis has shown that semilocal functionals yield a large overdelocalization error, which strongly affects the predicted high-pressure behavior, particularly the energetics of high-pressure phases. Hence, functionals that capture electron localization, such as hybrid functionals, are essential to study the high-pressure behavior of Ca. Furthermore, the computed electrical resistance with the HSE06 functional for fcc Ca shows satisfactory agreement with measured resistance data up to 30 GPa. Our findings are expected to be relevant for other alkali and alkali-earth metals that exhibit highly complex crystal structures at high-pressure conditions where the formation of such crystal lattices demands the existence of a two-component solid.

ACKNOWLEDGMENTS

P.M. and A.K.V. acknowledge the Computer Division, BARC, for providing the supercomputing facility. P.M.O. acknowledges support from the Swedish Research Council (VR, Grant No. 2018.05973) and the K. and A. Wallenberg Foundation (Grant No. 2022.0079).

[1] H. Fujihisa, Y. Nakamoto, M. Sakata, K. Shimizu, T. Matsuoka, Y. Ohishi, H. Yamawaki, S. Takeya, and Y. Gotoh, Phys. Rev. Lett. **110**, 235501 (2013).

[2] K. J. Dunn and F. P. Bundy, Phys. Rev. B **24**, 1643 (1981).

[3] H. Olijnyk and W. B. Holzapfel, Phys. Lett. A **100**, 191 (1984).

[4] T. Yabuuchi, Y. Nakamoto, K. Shimizu, and T. Kikegawa, J. Phys. Soc. Jpn. **74**, 2391 (2005).

[5] Q. F. Gu, G. Krauss, Y. Grin, and W. Steurer, Phys. Rev. B **79**, 134121 (2009).

[6] S. Anzellini, D. Errandonea, S. G. MacLeod, P. Botella, D. Daisenberger, J. M. De'Ath, J. Gonzalez-Platas, J. Ibáñez, M. I. McMahon, K. A. Munro, C. Popescu, J. Ruiz-Fuertes, and C. W. Wilson, Phys. Rev. Mater. **2**, 083608 (2018).

[7] S. Arapan, H.-K. Mao, and R. Ahuja, Proc. Natl. Acad. Sci. USA **105**, 20627 (2008).

[8] G. Gao, Y. Xie, T. Cui, Y. Ma, L. Zhanga, and G. Zou, Solid State Commun. **146**, 181 (2008).

[9] I. Errea, M. Martinez-Canales, A. R. Oganov, and A. Bergara, High Press. Res. **28**, 443 (2008).

[10] Y. Yao, D. D. Klug, J. Sun, and R. Martoňák, Phys. Rev. Lett. **103**, 055503 (2009).

[11] A. M. Teweldeberhan and S. A. Bonev, Phys. Rev. B **78**, 140101(R) (2008).

[12] T. Ishikawa, A. Ichikawa, H. Nagara, M. Geshi, K. Kusakabe, and N. Suzuki, Phys. Rev. B **77**, 020101(R) (2008).

[13] J. S. Tse, S. Desgreniers, Y. Ohishi, and T. Matsuoka, Sci. Rep. **2**, 372 (2012).

[14] M. Di Gennaro, S. K. Saha, and M. J. Verstraete, Phys. Rev. Lett. **111**, 025503 (2013).

[15] H. Liu, W. Cui, and Y. Ma, J. Chem. Phys. **137** 184502 (2012).

[16] A. R. Oganov, Y. Ma, Y. Xu, I. Errea, A. Bergara, and A. O. Lyakhov, Proc. Natl. Acad. Sci. USA **107**, 7646 (2010).

[17] R. J. Nelmes, D. R. Allan, M. I. McMahon, and S. A. Belmonte, Phys. Rev. Lett. **83**, 4081 (1999).

[18] T. Matsuoka and K. Shimizu, Nature (London) **458**, 186 (2009).

[19] Y. Ma, M. Eremets, A. R. Oganov, Y. Xie, I. Trojan, S. Medvedev, A. O. Lyakhov, M. Valle, and V. Prakapenka, Nature (London) **458**, 182 (2009).

[20] M. Marqués, G. J. Ackland, L. F. Lundegaard, G. Stinton, R. J. Nelmes, M. I. McMahon, and J. Contreras-García, Phys. Rev. Lett. **103**, 115501 (2009).

[21] M.-S. Miao and R. Hoffmann, J. Am. Chem. Soc. **137**, 3631 (2015).

[22] K. Takemura, N. E. Christensen, D. L. Novikov, K. Syassen, U. Schwarz, and M. Hanfland, Phys. Rev. B **61**, 14399 (2000).

[23] J. L. Dye, Science **247**, 663 (1990).

[24] H. G. von Schnering and R. Nesper, Angew. Chem. Int. Ed. Engl. **26**, 1059 (1987).

[25] S. Matsuishi, Y. Toda, M. Miyakawa, K. Hayashi, T. Kamiya, M. Hirano, I. Tanaka, and H. Hosono, Science **301**, 626 (2003).

[26] M. Hirayama, S. Matsuishi, H. Hosono, and S. Murakami, Phys. Rev. X **8**, 031067 (2018).

[27] D. Gregory, A. Bowman, C. Baker, and D. Weston, J. Mater. Chem. **10**, 1635 (2000).

[28] R. H. Huang, M. K. Faber, K. J. Moeggenborg, D. L. Ward, and J. L. Dye, Nature (London) **331**, 599 (1988).

[29] D. J. Singh, H. Krakauer, C. Haas, and W. E. Pickett, Nature (London) **365**, 39 (1993).

[30] R. F. W. Bader, Chem. Rev. **91**, 893 (1991).

[31] F. Hao, R. Armiento, and A. E. Mattsson, J. Chem. Phys. **140**, 18A536 (2014).

[32] G. Kresse and J. Furthmüller, Phys. Rev. B **54**, 11169 (1996).

[33] G. Kresse and J. Hafner, Phys. Rev. B **47**, 558 (1993).

[34] G. Kresse and J. Furthmüller, Comput. Mater. Sci. **6**, 15 (1996).

[35] P. E. Blöchl, Phys. Rev. B **50**, 17953 (1994).

[36] J. P. Perdew, K. Burke, and M. Ernzerhof, Phys. Rev. Lett. **77**, 3865 (1996).

[37] A. V. Krukau, O. A. Vydrov, A. F. Izmaylov, and G. E. Scuseria, J. Chem. Phys. **125**, 224106 (2006).

[38] A. Otero-de-la-Roza, E. R. Johnson, and V. Luãna, Comput. Phys. Commun. **185**, 1007 (2014).

[39] D. Alfè, Comput. Phys. Commun. **180**, 2622 (2009); also see http://chianti.geol.ucl.ac.uk/∼dario.

[40] C. Kittel, *Introduction to Solid State Physics* (John Wiley & Sons, New York, 2005).

[41] D. E. Gray, *American Institute of Physics Handbook* (McGraw-Hill, New York, 1972).

[42] A. Jayaraman, S. R. Shieh, S. K. Sharma, L. C. Ming, and S. Y. Wang, J. Raman Spectrosc. **32**, 167 (2001).

[43] C. Ji, V. I. Levitas, H. Zhu, J. Chaudhuri, A. Marathe, and Y. Ma, Proc. Natl. Acad. Sci. USA **109**, 19108 (2012).

[44] Y. Gao, Y. Ma, Q. An, V. Levitas, Y. Zhang, B. Feng, J. Chaudhuri, and W. A. Goddard III, Carbon **146**, 364 (2019).

[45] J. F. Cannon, J. Phys. Chem. Ref. Data **3**, 791 (1974).

[46] J. P. Perdew and Y. Wang, Phys. Rev. B **45**, 13244 (1992).

[47] See Supplemental Material at http://link.aps.org/supplemental/10.1103/PhysRevB.107.125152 for a table containing ambient-pressure properties; ELF isosurfaces for bcc and bct structures; NNM for fcc Ca below 8 GPa; lmto band structure character plots for fcc Ca; COHP functions and pressure variation of ICOHP for both fcc and sc Ca; and pressure variation of DOS at EF for fcc, sc, and bcc structures.

[48] V. G. Tsirelson, Can. J. Chem. **74**, 1171 (1996).

[49] S. G. Dale and E. R. Johnson, J. Phys. Chem. A **122**, 9371 (2018).

[50] M. Yu and D. R. Trinkle, J. Chem. Phys. **134**, 064111 (2011).

[51] T. E. Jones, M. E. Eberhart, and D. P. Clougherty, Phys. Rev. Lett. **105**, 265702 (2010).

[52] D. Errandonea, R. Boehler, and M. Ross, Phys. Rev. B **65**, 012108 (2001).

[53] R. Boehler, M. Ross, and D. B. Boercker, Phys. Rev. Lett. **78**, 4589 (1997).

[54] O. K. Andersen, Stuttgart TIGHT-BINDING LMTO program version 4.7, Max Planck Institut für Festkörperforschung.

[55] R. Dronskowski and P. E. Blöchl, J. Phys. Chem. **97**, 8617 (1993).

[56] A. B. Garg, V. Vijayakumar, P. Modak, D. M. Gaitonde, R. S. Rao, B. K. Godwal, and S. K. Sikka, J. Phys.: Condens. Matter **14**, 8795 (2002).

[57] P. B. Allen, in *Handbook of Superconductivity*, edited by C. P. Poole, Jr. (Academic Press, San Diego, CA, 2000), pp. 478–489.

[58] W. L. McMillan and J. M. Rowell, Phys. Rev. Lett. **14**, 108 (1965).

[59] P. B. Allen, Phys. Rev. B **36**, 2920 (1987).

[60] B. Nayak and P. Modak, Solid State Commun. **360**, 114993 (2023).